Coastal Engineering 179 (2023) 104243

Contents lists available at ScienceDirect

Coastal Engineering

journal homepage: www.elsevier.com/locate/coastaleng

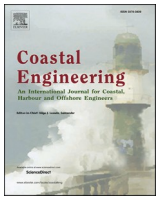

Numerical modeling of debris transport due to tsunami flow in a coastal urban area

Yu Chida [a,*], Nobuhito Mori [b,c]

[a] Tsunami and Storm Surge Research Group, Port and Airport Research Institute, Yokosuka, Kanagawa, 239-0826, Japan
[b] Disaster Prevention Research Institute, Kyoto University, Uji, Kyoto, 611-0011, Japan
[c] College of Engineering, Swansea University, Bay Campus, Fabian Way, Swansea, SA1 8EN, UK

ARTICLE INFO

Keywords:
Debris transport
STOC-DM
Local contact model
Sensitivity analysis
Numerical modeling

ABSTRACT

Many numerical models have been developed to estimate the behavior of debris generated by tsunamis. However, such numerical models have been validated through comparison with experimental data under simple conditions such as simple topography. Therefore, model applicability to actual topographic conditions such as ports and urban areas remains largely unknown. In this study, the modeling of contact with the seafloor and collision with buildings in an existing debris transport model (STOC-DM) is improved to enhance actual practical applicability. Moreover, debris numerical simulations are conducted using the results of hydrodynamic numerical simulations with different water level data obtained under the same wave generation conditions as used in the experiments, and the numerical results are compared with results obtained from debris experiments conducted in a previous study using a coastal urban model. The model improvements contribute to reproducing the statistical characteristics of debris position and the final arrival position; however, the modeled results on debris velocity cannot reproduce the experimental results. Therefore, sensitivity analysis is also conducted by applying disturbances not only to the fluid but also to the parameters of the debris model, e.g., drag coefficient, inertia coefficient, and friction coefficient. The combination results considering both disturbances improve the distribution of the debris velocity that cannot be reproduced using fluid disturbance alone.

1. Introduction

Tsunamis generated by megathrust earthquakes, such as the 2004 Sumatra, 2010 Chile, and 2011 Tohoku, can cause devastating damage to coastal areas (Mori et al., 2011; Borrero, 2005). Tsunamis with massive inundation cause huge hydrodynamic forces on structures and impact forces due to collision of water-borne debris (Riggs et al., 2014; Naito et al., 2014). Tsunami-related water-borne debris can be of various sizes and scales (e.g., vessels in ports, shipping containers stored in ports, vehicles, and houses in urban areas), and several formulas for the estimation of the impact forces on structures associated with such debris have been developed (Matsutomi, 1999; Ikeno et al., 2016; ASCE, 2016). However, water-borne debris transported onto land can cause not only direct damage owing to collision with structures but also indirect additional damage such as blocking routes for emergency evacuation and transportation through accumulation. Furthermore, debris damming occurring at openings between buildings is a concern for increased debris load (Stolle et al., 2018). Blocking routes can also occur at sea. For example, debris floating on the sea surface or sinking to the seafloor can block shipping routes and disrupt post-disaster port operations (Kumagai, 2013). To estimate the risk for future events, it is necessary to understand the process of water-borne debris diffusion from its origin and the extent of its impact.

Research to enhance our understanding of tsunami debris transport and diffusion has been conducted through field studies, laboratory experiments, and numerical simulations. Naito et al. (2014) conducted a field survey on the impact of debris on structures that occurred during the 2011 Tohoku tsunami. They also used Google Earth images to identify the final locations of shipping containers and vessels, and to estimate the "spreading angle" ($\pm 22.5°$) of the area of diffusion from the origin of the initial location. Their results are incorporated into the ASCE7-16 (2016) standard for assessing potential impact areas of tsunami debris.

Laboratory experiments on tsunami debris have been conducted by many researchers in recent years. Rueben et al. (2015) conducted a large-scale experiment using the Tsunami Wave Basin at Oregon State

* Corresponding author.
E-mail address: chida-y@p.mpat.go.jp (Y. Chida).

https://doi.org/10.1016/j.coastaleng.2022.104243
Received 11 August 2022; Received in revised form 30 September 2022; Accepted 25 October 2022
Available online 28 October 2022

University to obtain spatio-temporal data on debris by analyzing images of debris behavior on a flat floor. Their study showed that the variability in debris behavior during the leading wave was small. In contrast, debris behavior was varied during the return flow owing to the random nature of the current. Nistor et al. (2016) compared the results of experiments on debris behavior caused by tsunami-like inundation with the diffusion angle proposed by Naito et al. (2014), and proposed a stricter diffusion angle dependent on the number of debris objects. Additionally, Stolle et al. (2017) conducted repeated experiments by applying different hydrodynamic forces and orientations at an initial position. Their results showed that diffusion decreases as the hydrodynamic force increases, and that the diffusion and velocity of debris vary depending on the initial orientation. Furthermore, the formula for the debris diffusion angle proposed by Nistor et al. (2016) was modified to consider the effect of hydrodynamic forces. Stolle et al. (2019) conducted other experiments using different materials for the surface of the topography and for the debris to confirm the changes in debris behavior due to the effect of friction. Their results revealed no substantial change in the diffusion angle from the initial position and an effect on the transport distance in the downstream direction. Park et al. (2021) reported that the number of debris objects and the patterns of experimental conditions considered in previous experiments were too limited to represent the complex transport processes. Therefore, using a group of debris objects consisting of two objects with different densities, they conducted experiments by varying the number of objects, their arrangement, and the presence or absence of fixed objects to understand the characteristics of debris behavior. They showed that if the percentage of lightweight debris objects is large, the displacement of the debris is small and exhibits little variability.

Knowledge of the basic characteristics and variability of debris behavior has been accumulated through various previous experiment-based studies. However, as highlighted by Kihara and Kaida (2020), tsunami inundation phenomena are highly localized. Moreover, it has yet to be fully confirmed whether the obtained knowledge, such as the formulas used for estimating variability, is applicable to actual regions with various scales and different numbers of structures. Regarding interference by structures, Kaida and Kihara (2016) reported the effect of reflected waves from the front of a structure that was approximately 10 times larger in scale than the debris on the collision velocity and collision probability of debris on the structure. In Kihara and Kaida (2020), based on the experimental results of Kaida and Kihara (2016), the effect of reflected waves was appropriately included in an investigation of debris behavior by adding a bore wave model (Kihara and Kaida, 2019) to the hydrodynamic model of a debris transport model developed by themselves. Goseberg et al. (2016) reported that the effect of a fixed obstacle is small for the spreading angle parameter on the basis of their experimental results. However, the structures and debris objects used in their experiments were of similar scale, suggesting that the effect of structures on debris motion might be relatively small. Park et al. (2021) conducted debris experiments with a varying number of structures that were four times larger than the debris. They found that an increase in the number of structures did not affect the spreading angle or movement in the downstream direction. They further noted that the influence of local conditions such as structures on debris behavior represents a subject for future research.

Numerical studies have been conducted so far using numerical models that can track the behavior of moving debris (Goto, 1983; Fujii et al., 2005; Ayca and Lynett, 2021). These debris transport models can track debris behavior associated with tsunami flow by modeling the drag force, inertia force, collision force, and friction force acting on the debris. It is also possible to consider the interaction between the debris and the fluid, as performed by Kihara and Kaida (2020) and Ayca and Lynett (2021). Numerical simulations can represent changes in local tsunami flow attributable to structures and local topography, and track the behavior of the tsunami debris that follows the local flow. Park and Cox (2019) and Chida and Takagawa (2019) have applied debris transport models to actual regions, and have addressed the prediction or reproduction of the volume and the final location of debris derived from the destructed buildings. The accumulation of these results is necessary to establish debris management (e.g., The Federal Emergency Management Agency, 2007) for the early recovery of communities from disasters. However, the applicability of debris transport models to actual areas has not been studied adequately because the validation of debris transport models is generally based on benchmark data obtained from experiments conducted under simple conditions. Another factor that makes the validation of debris transport models difficult is the problem of obtaining spatio-temporal data of debris motion, other than Automatic Identification System (AIS) data, during an actual tsunami.

When evaluating the forces acting on debris in a debris transport model, values for the level and velocity of the water simulated by the hydrodynamic model are needed. Therefore, when conducting validation of a debris transport model, the accuracy of the hydrodynamic model must be guaranteed as a precondition. In recent years, comparisons between laboratory experiments using scaled physical models and the results of hydrodynamic numerical models have been conducted (Park et al., 2013; Fukui et al., 2022). For example, in a study conducted by the author's group (Fukui et al., 2022), time series data of inundation extent obtained by image analysis and surface current velocity data obtained via particle image velocimetry (PIV) analysis were used to validate the accuracy of the hydrodynamic models (Fukui et al., 2022; Chida et al., 2021). Furthermore, Chida et al. (2020) conducted debris experiments using the same 1/250 scale physical model used by Fukui et al. (2022). They obtained spatio-temporal data to examine the effects of building groups and bathymetry with distribution. Their experiment was the first attempt in the field to use a physical model based on actual topography and bathymetry. Chida et al. (2021) compared their experimental results with results obtained using the STOC-DM numerical debris transport model. They found that local contact between the bottom of debris objects and the seafloor has a significant influence on debris motion immediately after initiation of movement, suggesting the need for further model improvement.

In this study, a debris transport model is improved to consider local contact between the bottom of debris objects and the seafloor. The performance of the improved model is evaluated, and sensitivity analysis is conducted for the important parameters of the debris transport model. An overview of the physical model experiments is given in section 2. An outline of the numerical simulations and a description of the improved model are given in section 3. The numerical results are presented in section 4, and discussions of the effects of the model improvements and the results of the sensitivity analysis are given in section 5. Finally, our conclusions are presented in section 6.

2. Physical modeling

Debris experiments were conducted using the Hybrid Tsunami Open Flume in Ujigawa laboratory (Hy TOFU) at the Disaster Prevention Research Institute (Kyoto University, Japan). The length of this flume was 45 m and its width was 4 m. This flume could generate tsunami-like long and irregular short waves using a combination of a water pump, piston-type mechanical wavemakers, and a dam-break-gate wave generator (Hiraishi et al., 2015). The 70-kW pump could generate a time series of water levels similar to that of a tsunami or a storm surge waveform by discharging flow via a pair of 2×0.2 m outlets at the flume bed. The maximum pumping capacity was 0.83 m^3/s with a maximum operating time of 1200 s. The piston-type mechanical wavemaker had a 2.5-m maximum stroke and maximum speed of $\leq$2.83 m/s. The wavemaker could generate multiple wave types, including solitary, regular, or irregular waves at frequencies lower than 2 Hz (Tomiczek et al., 2016).

To understand the characteristics of debris behavior in complex flows, a wooden model of part of the city of Kainan (Wakayama Prefecture, Japan), including the port, buildings, and houses, was used in

this series of experiments. Fig. 1 shows the location of the study area, and Fig. 2 shows plan and side views of the physical model. The city model, which was constructed at 1/250 scale and covered an area of the center of the city that extended 2 km from east to west and 1 km from north to south, reproduced not only the distribution of buildings but also that of water depth in the port. This area is considered vulnerable to damage by tsunamis triggered by earthquakes on the Nankai Trough. The physical city model was installed on a steel plate 0.8065 m above the bottom of the water flume on a 5.5-cm wooden base. This physical model was connected to the water of uniform depth by a slope with a gradient of 1:10. The still water depth used in the experiments was 0.877 m (Fukui et al., 2022).

The debris object used in the experiments was a rectangle with width of 0.1 m, length of 0.25 m, height of 0.1 m, and specific gravity of 0.25, which was created using a 3D printer (MakerBot Replicator Z18), as shown in Fig. 3. The length of the debris object is 62.5 m at full scale. This is roughly the same as the 54 m length of the 18th Kyotoku Maru (Suga et al., 2013), which was stranded in the city of Kesennuma in the 2011 Tohoku tsunami. Moreover, we selected the rectangle shape for the debris experiment because the shape modeled in the debris transport model is a rectangle, as described in subsection 3.1. The debris behavior in the city model was captured using a 4K video camera installed on top of the tank. The change in debris position over time was obtained by tracking five markers attached to the top surface of the debris using image analysis software (DIPP-Motion Pro 2D). The rotation angle of the debris was estimated based on the locations of the markers. One debris object was installed on land and one was installed in the water, as shown in Fig. 3. The debris in the water was placed in contact with the seafloor to fix its initial position. The experimental procedure was repeated 10 times under the same conditions to confirm the reproducibility of debris behavior.

The leading wave of the tsunami-like long wave used in the experiments was generated for 5 min by fixing the pump flow rate at 0.035 m^3/s and then the return flow for 2 min was generated by stopping the pump flow. Two wave gauges (WG1 and WG2) were installed in the flume to measure water surface elevation during the experiments. WG1 was installed near the wave generator to make the initial wave conditions for use in the numerical simulation, and WG2 was installed near the mouth of the port entrance, as shown in Fig. 2. The maximum water surface elevation in this experiment was 0.063 m, which represents a height of 15.80 m at full scale. The time series of all water surface elevations

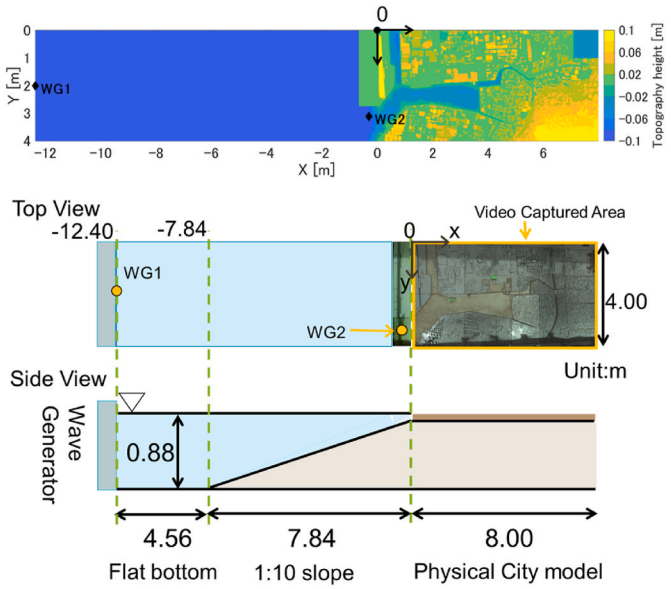

Fig. 2. Computational domain (upper), top view (center), and side view (lower) of the physical model and initial locations of the debris (green rectangles), taken from Fig. 2 from Fukui et al. (2022). Circles labeled WG1 and WG2 identify the locations of the wave gauges, and yellow rectangle shows the video-capture area.

measured at WG1 in each run showed good repeatability. The standard deviation of the ensemble was approximately 1 mm throughout the entire waveform, indicating that the variation in water surface elevation between experiments was small.

Before conducting the debris experiments, tsunami propagation and inundation experiments were conducted under different wave conditions. Twelve wave gauges were installed to obtain time series data of water surface elevation. Furthermore, fluorescent red dye was injected into the water area before wave forcing to detect the leading edge of the inundation. Additionally, the flow pattern was measured using 5-mm particles painted with fluorescent yellow dye in the selected case for PIV analysis. These results have already been published (Fukui et al., 2020, 2022).

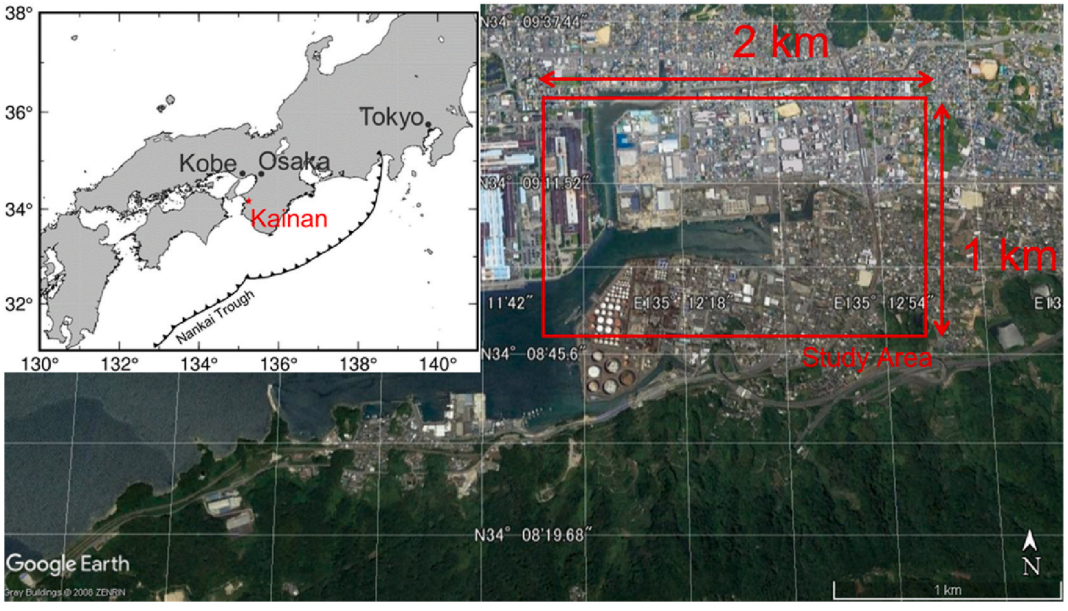

Fig. 1. Location of Kainan city (upper left) and overview of the coastal city area used as a study area (red box), revised Fig. 1(a) in Fukui et al. (2022).

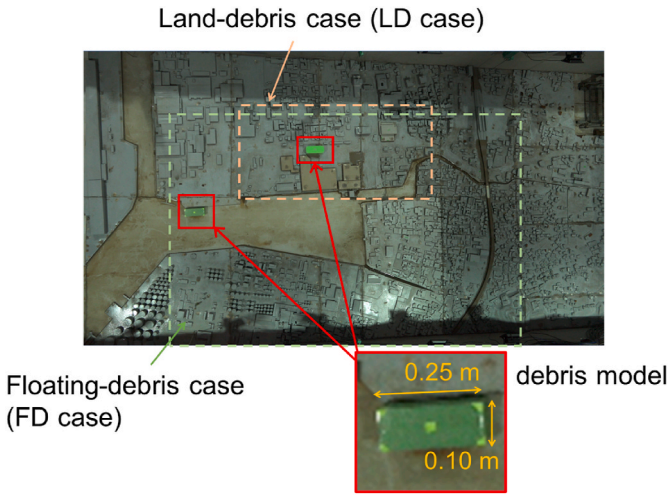

Fig. 3. Zoomed-in view of the physical city model and initial locations of the debris (red rectangles).

3. Numerical modeling

3.1. Outline of the numerical model

This study used sub-models of the Storm surge and Tsunami simulator in Ocean and Coastal areas (STOC) model (Tomita and Kakinuma., 2005). The STOC-ML model is a multilayer hydrostatic approximation model that was used to simulate tsunami propagation and inundation. The governing equations are the Reynolds Averaged Navier–Stokes equations, but in this study, the Reynolds stress was neglected and the total number of vertical layers used was one. Therefore, it was equivalent to the conventional shallow water equations used in general tsunami numerical models.

The STOC-DM model was used to simulate debris behavior. The debris is modeled as a rectangular rigid body, and the behavior of the debris object is simulated based on Newton's second law with four degrees of freedom. The translational motion and rotational motion around a vertical axis through the object center are simulated based on the following equations of motion:

$$m\alpha = F_{flow} + F_{frc}, \tag{1}$$

$$I\frac{d\omega}{dt} = T_{flow}, \tag{2}$$

where m, I, α, and ω are the mass, moment of inertia, acceleration vector, and angular velocity around a vertical axis of the debris, respectively. Variable F is a vector of external forces acting on the debris, and variable T is the torque around the vertical axis. The subscript "flow" means the hydrodynamic force and the subscript "frc" means the friction force. The translational motion in the vertical direction follows the tsunami height while maintaining the draft depth of the debris. Therefore, if the tsunami height is smaller than the draft depth, the bottom of the debris remains in contact with the seafloor or ground surface and F_{frc} is active. F_{frc} is simulated by

$$F_{frc} = -\mu(m - \rho_w LBh)g, \tag{3}$$

where μ, ρ_w, L, B, and h are the coefficient of kinetic friction, density of water, the length of debris, the width of debris, and water depth at the center of gravity, respectively. Evaluation of the hydrodynamic force F_{flow} and T_{flow} is based on the method of Ikeya et al. (2005), which is an extension of the Morrison equation and simulated as the sum of the drag force and the inertia force. In the study of Ikeya et al. (2005), the accuracy of evaluation equations was validated by comparing with experimental data. The coefficient of drag force and inertia force in the evaluation equations used in their validation is also adopted in STOC-DM. Other detailed explanations regarding STOC-DM can be found in the previous study (Tomita and Honda, 2010).

3.2. Improvement of friction model

In STOC-DM, if the height of the bottom of the debris object is at the same height as the topography or if the water depth is equal to the draft depth, contact between the debris bottom and the seafloor or ground surface is detected. This detection is performed for each debris. After detection, the friction force is evaluated, assuming that the entire debris bottom contacts with the surface. Because the friction force is represented at the center of gravity, the friction force for translational motion can be considered. However, the attenuation of rotational motion due to friction is not calculated (Fig. 4).

Image analysis of the video data obtained in the experiments showed that local contact between the bottom of the debris and the seafloor caused rotational motion around the axis of a local contact position, not the axis through the center of the object. Therefore, in this study, we added a friction term to the motion equation for rotation and modeled it for the motion constrained to a local contact position. First, we explain how the friction term for rotational motion is handled in STOC-DM. As described above, STOC-DM represents a debris object as a single element with a rectangular body. This is different from numerical models such as the Discrete Element Method (DEM) (Xiong et al., 2022) that represent the shape of debris as a combined body of individual elements. For a shape composed of multiple individual elements, it is possible to represent a situation where the object is locally in contact with the ground by comparing the height of the individual elements with the height of the ground surface. The friction force acting on the contacting individual elements can be simulated in such cases. Therefore, we added a procedure to STOC-DM to estimate the overlap region between the object and the computational grid, and to detect the contact by comparing the height of the ground and the bottom height at each computational grid. Thus, contact determination is conducted at each computational grid in the overlap region. The summation of the friction force for translational motion and the summation of torque reduction due to the friction force can be simulated. F_{frc} in improved model is simulated by Eq. (4) and Eq. (5):

$$F_{frc} = \sum_{i,j} F_{frc,i,j} \tag{4}$$

$$F_{frc,i,j} = \begin{cases} -\dfrac{S_{i,j}}{LB}\mu\left(m - \rho_w LBh_{i,j}\right)g, & h_{i,j} < \text{draft depth} \\ 0, & h_{i,j} \geq \text{draft depth} \end{cases} \tag{5}$$

where $S_{i,j}$ and $h_{i,j}$ are the overlap area at each computational grid and the water depth at the center of the overlap area at each computational grid.

The above improvements can account for frictional attenuation of the rotational motion. However, the model still cannot account for the shift of the axis for rotational motion and the associated rotational motion caused by local contact with the seafloor surface, as confirmed by experiments. This is because the equation of motion for debris rotation, which is also used in STOC-DM, is constructed as rotation around an axis through the object center. Generally, the equations of motion and the force acting on a debris object do not change for translational motion, even if the center of gravity is at any location. Nevertheless, the torque does change because the distance between the position of force action and the center of gravity changes. Therefore, we introduced a local contact model that solves for the rotational motion around the shifted axis obtained by simulating the position of the center of contact area between the debris bottom and the seafloor when the following condition is satisfied:

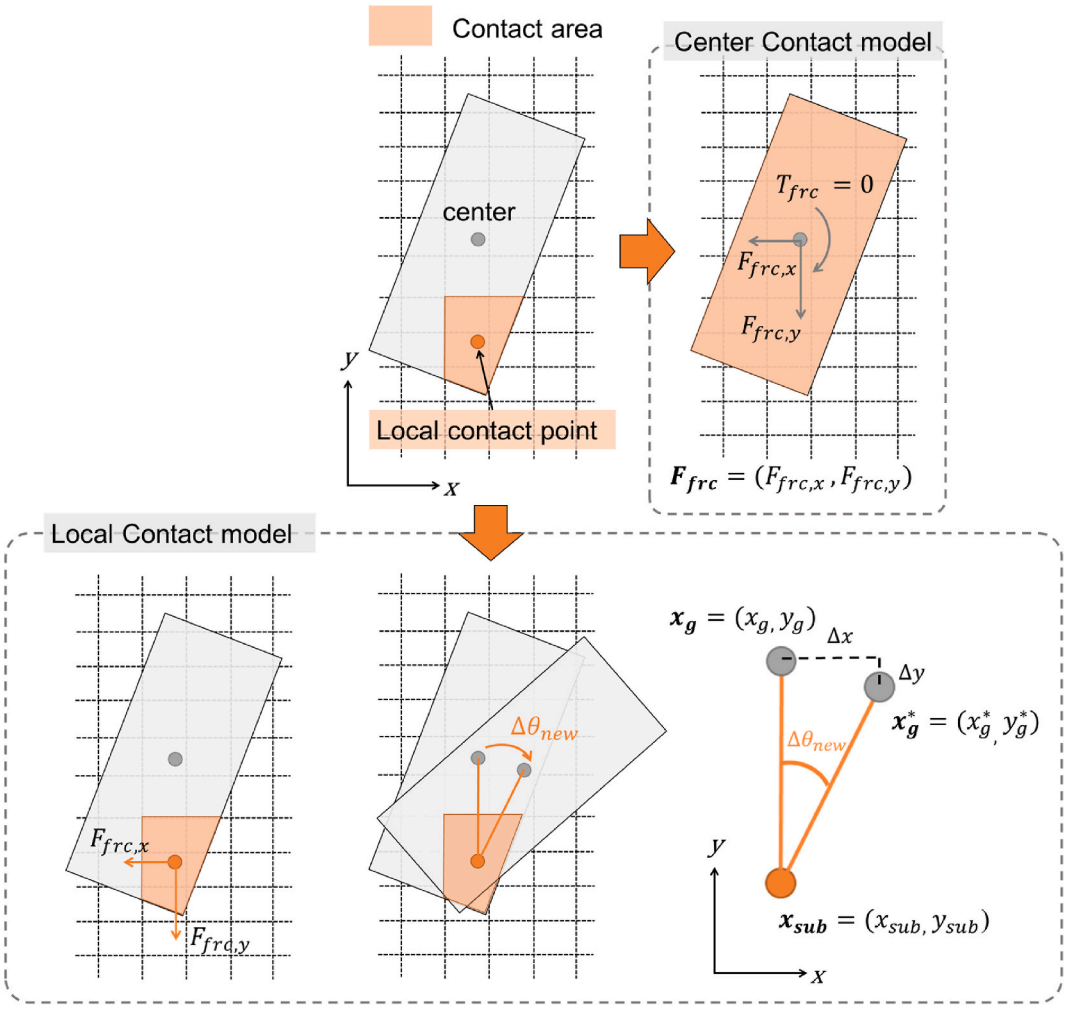

Fig. 4. Schematic of the difference between the center contact model (upper right) and the local contact model (lower).

$$\omega^n \omega^{n+1} \leq 0 \; and \; T'^{\,n}_{flow} T'^{\,n+1}_{flow} \geq 0 \; and \; \left|F_{flow}\right| - \left|F_{frc}\right| \leq 0, \tag{6}$$

where T' is the value of torque without friction and subscript n is the time step. This condition expresses the situation where the rotational motion around the axis through the object center stops owing to friction caused by local contact with the seafloor, although the torque without friction T' acts in the same direction between time step n and the next step, and the external force F_{flow} is less than the friction force F_{frc}. In other words, this condition indicates that if rotational motion is stopped by friction and translational motion is also decelerated by friction, the rotation axis shifts. In contrast, if the debris is accelerated in the translational direction, the local contact does not affect the object sufficiently to shift the rotation axis.

When this condition is satisfied, the torque around the shifted rotation axis is simulated, and the rotation angle $\Delta\theta_{sub}$ is simulated by solving the equation of motion using the new moment of inertia and new torque. As mentioned above, the hydrodynamic force F_{flow} is not affected by a change in the position of the rotation axis, but as shown in Fig. 4, the position of the object center is changed owing to the rotation around the shifted axis. This shift of the object's center position Δx_{sub} is calculated as follows:

$$\Delta x_{sub} = x_g^* - x_g^n, \tag{7}$$

$$x_g^* = x_{sub} + R\left(x_g^n - x_{sub}\right), \tag{8}$$

where x_g^* and x_{sub} represent the vector of the position of the object center shifted by the rotational motion around the shifted axis and the vector of the position of the shifted axis in fixed coordinates, respectively. Note that x indicates the position in the fixed coordinate system. R is a transformation matrix around the shifted axis, which is calculated as follows:

$$R = \begin{pmatrix} \cos\Delta\theta_{sub} & -\sin\Delta\theta_{sub} \\ \sin\Delta\theta_{sub} & \cos\Delta\theta_{sub} \end{pmatrix}. \tag{9}$$

Finally, the position of the object center at the next time step is given by the following:

$$x_g^{n+1} = x_g^n + \Delta x_g + \Delta x_{sub}, \tag{10}$$

where Δx_g is the shift of the object center obtained by solving Eq. (1).

3.3. Improvement of the collision model

The results obtained using the collision model before its modification are discussed in a later section; however, it was found that the unmodified STOC-DM (Tomita and Honda, 2010) could not maintain a non-contact condition for debris colliding with multiple buildings at the same time. Therefore, we improved the collision procedure for multiple collisions between a single piece of debris and buildings by repeating the conventional momentum correction and position correction with the modified momentum (Ayca and Lynett, 2021). For the collision

response, the momentum conservation equations at the collision point are solved to obtain the post-collision and angular velocity. The steps of the computational flow adopted for the collision process are as follows.

1. Detect collision determination; if a collision occurs, proceed to step 2.
2. Evaluate the modified momentum based on the momentum conservation equations in the same way as Ayca and Lynett. (2021).
3. Correct the position based on the corrected momentum.
4. Return to step 1 and perform collision detection until a non-contact condition is determined.

Although it might depend on various conditions, such as the timestep and the scale difference between the debris and the building, it was found that the non-contact condition could be maintained in this case if the process was repeated approximately 5–10 times. Note that the time step used in the collision procedure was the same as the time step used to solve the motion equations for debris.

3.4. Numerical setup

Fig. 2 shows the topography and bathymetry of the computational domain. Elevation data for the physical city model ($X > 0.0$ m) were created by interpolating scanned point cloud data into grid data. Point cloud data were obtained using a laser scanner (Leica BLK360) set up at three locations in the basin, with the results combined into a single dataset. The horizontal grid size was set to 1 cm, which resulted in a domain of 2037 $\times$ 400 points. Bottom roughness was based on the Manning model with roughness coefficients of $n = 0.025$ for $X < -0.66$ m and $n = 0.013$ for the domain of the physical city model ($X > -0.66$ m) based on land usage following Kotani et al. (1998).

The water surface elevation measured at the location of WG1, as shown in Fig. 2, was used as the condition for the incident boundary on the west (ocean) side of the computational domain. A free transmission condition was applied at the open boundary on the east side. A wall boundary with a slip condition was used at the north and south side boundaries. The period for the numerical simulation was set to 420 s (7 min), which was the same as adopted in the experiment, and the duration of the return flow was also included in the numerical simulation.

One debris object was installed on land (hereafter, land-debris case (LD case)) and one was installed in the water (hereafter, floating-debris case (FD case)). The specifications of the debris objects were the same as in the experiment. The initial positions and angles of the debris objects were the average values of the center positions and angles obtained from the image analysis results. The debris starts to move when the height from the debris bottom to the water level at the debris center becomes larger than the draft depth. In this numerical simulation, feedback from debris to the fluid was not considered. Ten cases of the hydrodynamic numerical simulation were conducted using the water surface elevation data obtained from 10 repeated experiments as boundary conditions. The initial positions and angles of the debris were the same in each of the 10 numerical simulations.

4. Results

4.1. Comparison of flow fields

The validation of the numerical results of the fluid field is important because debris motion is strongly affected by flows. Fig. 5 compares the numerical and experimental time series of water surface elevation at WG2, located at the entrance to the mouth of the port. Because of the large number of simulated cases, the average values and standard deviations are shown in Fig. 5. The comparison reveals that the numerical results of tsunami propagation to the mouth of the port from WG1, which is located near the wave generator, agree with the experimental results. Unfortunately, no data on water surface elevation at any wave gauges or visualization results of the inundation extent or PIV analysis were obtained on the city model for the same wave generation case as the debris experiments. However, detailed comparisons with experimental data obtained in other wave cases were conducted in previous studies (see details in Fukui et al., 2022; Chida et al., 2021). A solitary wave of 0.05 m height was used in the study of Fukui et al. (2022), and the time scale of the tsunami was 30 s. In the study of Chida et al. (2021), the condition of wave generation was similar to that of this study, which the pump flow rate was at 0.025 m^3/s and the time scale for the leading wave and return flow was the same. The maximum wave height was 0.043 m. The previous results indicated that the STOC-ML model used in this numerical simulation could reproduce not only the time series of water levels measured by the wave gauges but also the changes over time in terms of the inundation extent and the presence of large-scale eddies generated at the inner part of the port under both wave conditions. The following provides a brief summary of the flow field.

The incident flows and inundation processes are important because they are directly related to the debris behavior discussed in the following sections. The height of the land or the port above the initial water level along the shoreline is approximately 1 cm. The water surface level in the channel exceeds 1 cm approximately 30 s after the start of the experiment, as shown in Fig. 5. After 30 s, inundation commences in the northeast direction at the shoreline near the initial location in the FD case and in the south direction at the southeast corner of the channel near Channel B shown in Fig. 6. Note that the upper direction in Fig. 6 indicates the north (negative to y) direction. The continuous flow propagates with further increase of the water level, and the flow direction does not change from the beginning of the inundation. In the

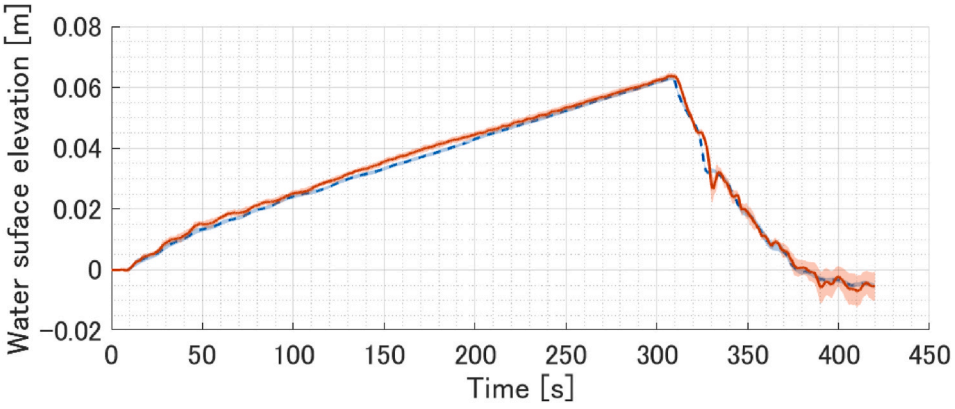

Fig. 5. Comparison of time series of water surface elevation at WG2 located at the mouth of the bay (as shown in Fig. 1(b)). (Line: average value of all results, colored area: standard deviation, blue: experimental data, red: numerical results).

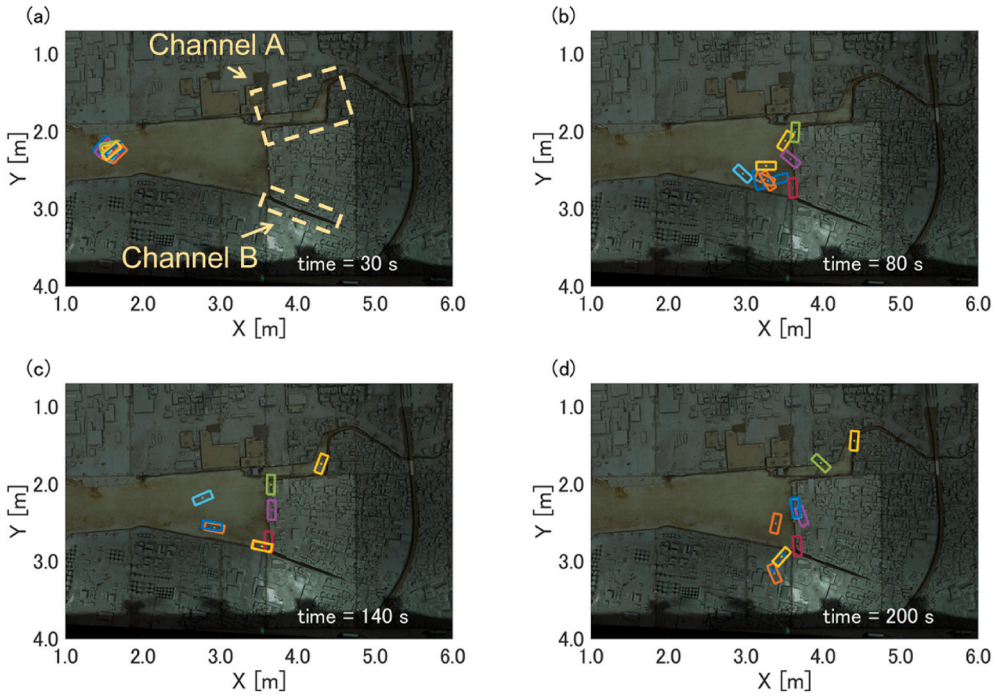

Fig. 6. Snapshot of debris behavior in the experiment in the FD case. (a) 30 s, (b) 80 s, (c) 140s, and (d) 200 s (color boxes: positions of debris).

channel, vortices continuously generated by the separation flow at the port entrance are simulated to be transported to the inner part of the channel. The patterns of flow and inundation are similar to the experimental results conducted under different wave generation conditions (Fukui et al., 2020; Chida et al., 2021).

4.2. Comparison of floating-debris movements

We describe the differences in the debris behavior in the FD case obtained from both numerical models. The numerical model that considers the contact process only at the center of gravity and a single collision is denoted the 'Center Contact + Single Collision' model (hereafter, the CC + SC model). Similarly, the numerical model that considers the process of local contact and multiple collision points is denoted the 'Local Contact + Multiple Collision' model (hereafter, the LC + MC model).

First, we discuss the rotational motion of the debris in the initial stages of movement and the subsequent direction of movement in the channel. Fig. 6 shows a time sequence of the experimental results of debris positions, and Fig. 7 shows a time sequence of the numerical results of debris positions. In the CC + SC model, in the first 30 s, all debris moves in the channel while maintaining its initial angle (Fig. 7 (a)). Conversely, the debris in the LC + MC model moves in the southeast direction with a counterclockwise rotation from the initial state (Fig. 7 (b)). The rotational motion in the initial stage and the direction of movement from the initial position are similar to the experimental results. The total water depth does not exceed the draft depth of debris until 40 s in the vicinity of the initial position (Fig. 8). This means that the contact with the seafloor is repeated until 40 s, and causes the difference in the rotation angle between the CC + SC model and the LC + MC model at the initial stage of the movement. The debris arrives at the shoreline on the east side of the channel 80 s after the start of the numerical simulation. It accumulates in two main locations after approximately 110 s: the north channel (hereafter, Channel A) and the small south channel (hereafter, Channel B). The locations of the two channels are shown in Fig. 6. Although debris reaches these two major locations in both numerical models, there are differences in debris accumulation. In the CC + SC model, 6 out of 10 debris objects accumulate in Channel A (Fig. 7(c) and (e)), while only 4 accumulate in the LC + MC model (Fig. 7(f)). In the experiment, only 2 out of 10 debris objects accumulate in the channel (Fig. 6(b) and (c)). The consideration of the local contact between the debris and the seafloor leads to the improvements in terms of initial rotation and number of accumulations in the LC + MC model relative to the CC + SC model. The changes in the initial rotation angle and the direction of movement are described in detail in the Discussion section.

In the CC + SC model, all debris in Channel A moves onto the land area located north of Channel A after approximately 140 s, and passes between buildings or stops at the group of buildings. This behavior is more evident in Fig. 9, which illustrates the trajectories of debris objects from the beginning of their movement to their final position at the end of the leading wave (300 s). One debris object drifts near the station, which is a location similar to the final position of some debris in the experiments. However, this behavior should not occur in the CC + SC model because the water level around the group of buildings is lower than the top of the buildings and the road around this area is narrower than the debris size. In the LC + MC model, 2 debris objects move into Channel A and drift near the station. The trajectories and final positions of the debris are similar to those of the experiment results. The other two debris objects move onto the land area located north of Channel A, as in the CC + SC model, but these debris objects never pass between the buildings. This behavior occurs because the revised collision model can maintain the non-contact condition with the buildings.

In the experiment, some debris in contact with the southern shoreline moves in response to large vortices generated at the inner part of the bay from 140 s (Fig. 6(b) and (c)). No such behavior is simulated by either of the numerical models except for one debris in LC + MC model as shown in Fig. 7(c). However, even this debris is affected by the vortex at different locations: the center area of the bay in the numerical simulation, and the inner part of the bay in the experiment. In the CC + SC model, the debris is already on land at that time and is unaffected by the current due to the vortices (Fig. 7(e)). This movement to the land area is unnatural because it occurs before the inundation depth at the land area is smaller than the draft depth. In contrast, in the LC + MC model, debris is unaffected by the current owing to its accumulation near the entrance to channel B (Fig. 7(f)). However, the debris in the LC + MC model

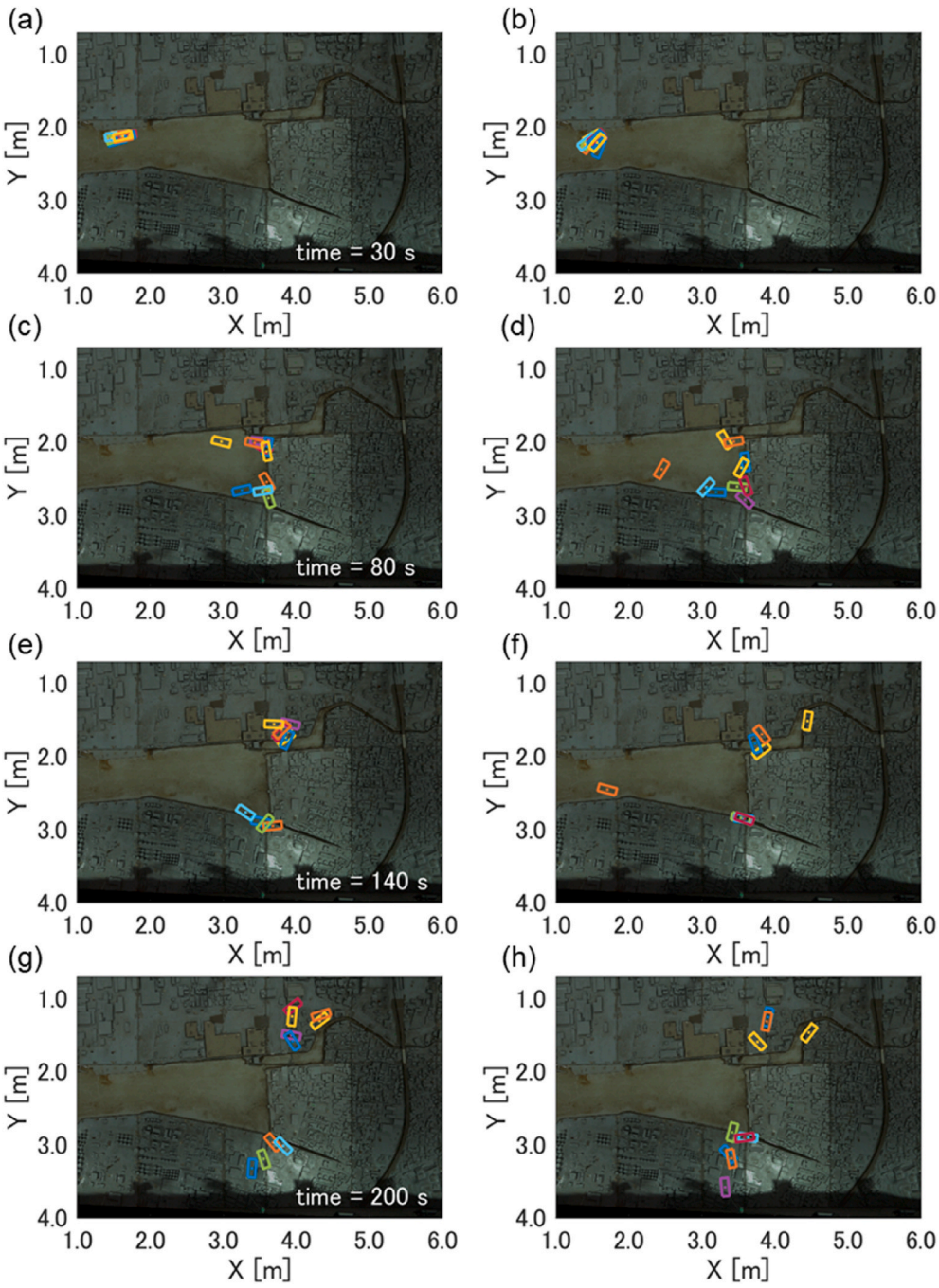

Fig. 7. Snapshot of modeled debris behavior in the FD case at 30, 80, 140, and 200 s (color boxes: positions of debris, left column: CC + SC model, right column: LC + MC model).

maintains the non-contact condition with the shoreline and remains in the sea area until the water level is sufficiently high for it to move onto the land area because of the improved collision model. Consequently, the movement from the sea onto the land occurs between 140 and 170 s after the start of the numerical simulation (Fig. 7(f) and (h)), which is similar to the experimental results. Furthermore, the arrival position in the LC + MC model is also close to that in the experimental results (Fig. 7 (h)). These results indicate that the development of the local contact model and the revised collision model improves the initial rotational motion and, consequently, the trajectories and final positions of the debris.

4.3. Comparison of land-debris movements

The land-debris behavior is more complex than that of the floating debris. The difference in debris behavior between both numerical models is discussed for the LD case in this section. First, we compare the starting time of movement. Fig. 10 shows a time sequence of the experimental results of debris positions, and Fig. 11 presents snapshots of the modeled debris position. Most of the debris starts to move after 180–190 s in both numerical models as shown in Fig. 8. In contrast, most of the debris starts to move after approximately 200 s in the experiment. Therefore, the average value of the inundation depth in the numerical results at the initial position of the debris is 0.0275 m at 200 s when the debris starts to move in the experiment, whereas the inundation depth

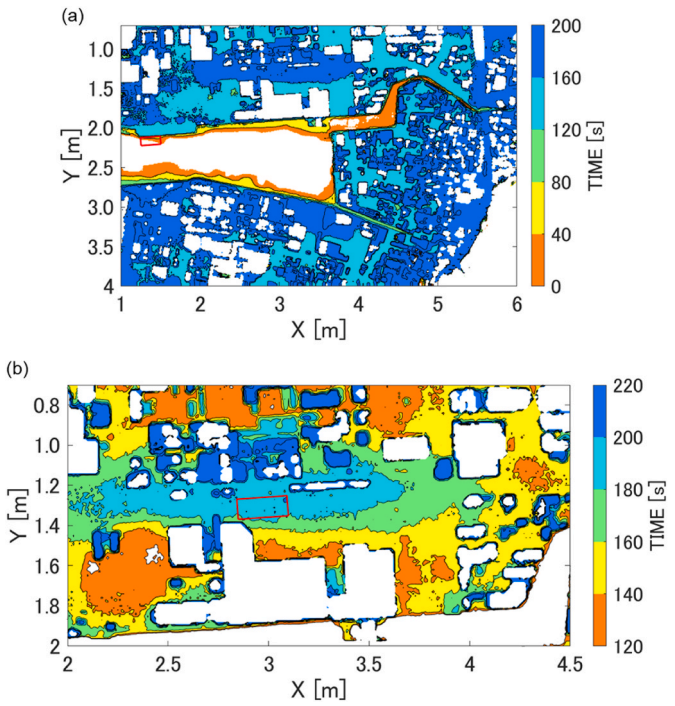

Fig. 8. The time when the total water depth exceeded the draft depth of debris. (a): FD case, (b): LD case. (Contour: Time, Red rectangle: initial position of debris).

for the start of movement in the numerical simulations is 0.025 m, i.e., the same as the draft depth. This means that there is a 10% error concerning the inundation depth. One reason for this discrepancy may be related to uncertainty in the draft depth of the debris. However, it is also possible that the momentum attenuation attributable to the friction term in the momentum equation in the STOC-ML model is underestimated because the numerical model overestimated both the extent of inundation deep in the city model and the run-up velocity of the tsunami edge in previous studies (Fukui et al., 2022).

Next, we describe the process from the start of debris movement to collisions with the group of buildings in the eastward direction. The debris moves in the eastward direction owing to the eastward inundation flow at the shoreline near the initial location of the FD case (Fig. 11 (a) and (b)). Some debris collides with a building to the south that obstructed movement in the eastward direction (Fig. 11 (c) and 11(d)). This collision occurs in the experiment and in the numerical simulations. Fig. 12 shows the trajectories of debris with arrival positions at 300 s when the flow direction changes from the leading wave to the backwash flow. The difference between the two types of lines in this figure indicates that the debris passes through the intersection of the east–west and north–south roads (white dotted line) at different times. In the experiment (Fig. 12(a)), debris collides with a building to the south and passed through the intersection after 250 s, which means that the collision causes a delay in the eastward movement. In the numerical models (Fig. 12(b) and (c)), most debris passes through the intersection before 250 s, even if collision with the building to the south occurs. Furthermore, some debris exhibits minimal movement from the initial position, even at the end of the leading wave, irrespective of the model improvement (Fig. 11(g) and (h)). This result is inconsistent with the experimental results. Fig. 13 shows the velocity vector of the flow field focused on the vicinity of the initial position of the debris in the LD case. This shows that a strong vortex is continuously generated near the initial position of the debris. Thus, debris caught in the vortex would continue to remain near the initial position. These discrepancies might be attributable to the accuracy of the inundation process on the land area, as mentioned in relation to the discrepancy in the starting time of movement.

Finally, we compare the experimental and numerical results for the collision process with the group of buildings in the eastward direction. In the experiment, all debris is captured by these buildings (Fig. 12(a)), even if the time of passing the intersection differs. However, interestingly, debris that passes the intersection before 250 s (i.e., the debris that

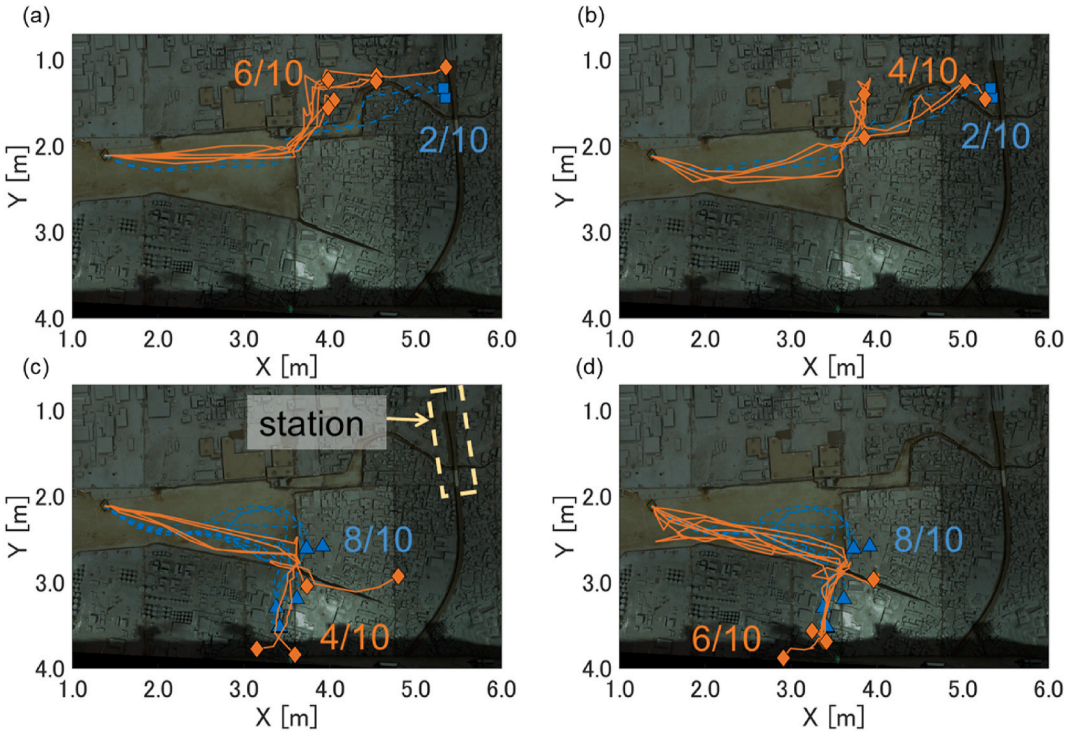

Fig. 9. Comparison of object trajectories between experiment and numerical results (colored markers: positions of debris at 300 s (end of leading wave), numbers: arrival numbers in each area, blue dotted line: experimental results, solid red line: numerical results, left column: CC + SC model, right column: LC + MC model).

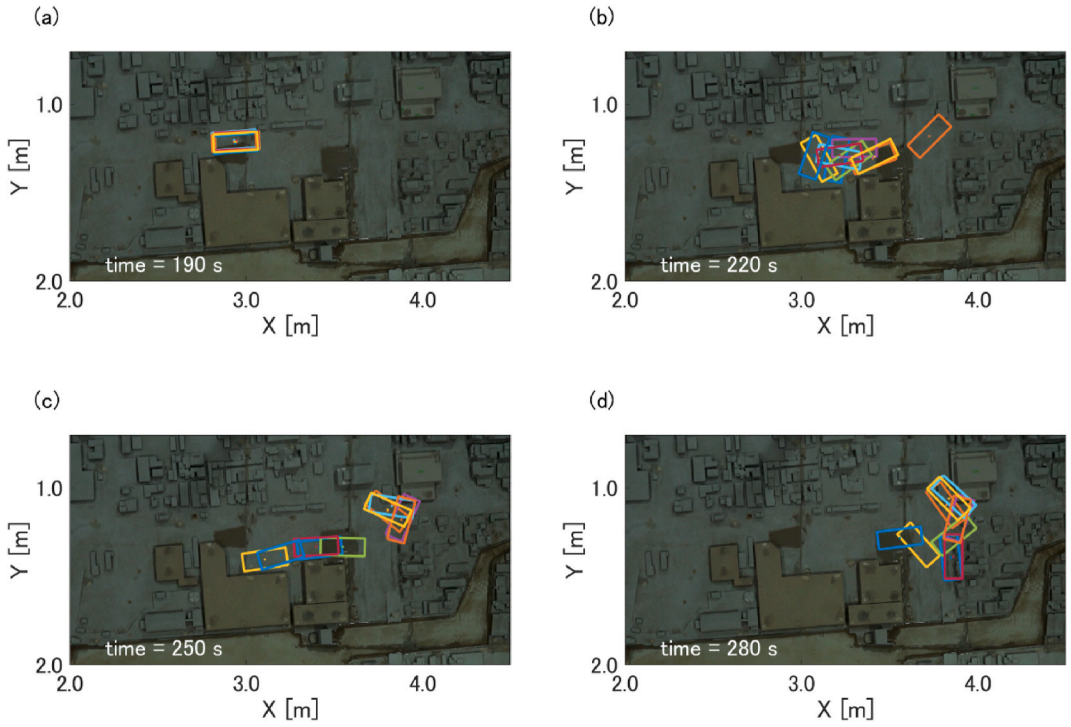

Fig. 10. Snapshot of debris behavior in the experiment in the LD case. (a) 190 s, (b) 220 s, (c) 250 s, and (d) 280 s (color boxes: positions of debris).

reaches these buildings directly from the start of the movement, shown by the solid line in Fig. 12(a)) is caught on the north side of the buildings. In contrast, as shown by the dotted line, other debris is caught on the south side of the buildings. The reason for this is unclear because no spatio-temporal data were obtained on the flow under the same wave conditions. There is a possibility that the intensity of the flow in the north–south direction changes at around 250 s. Namely, the eastward flow and the northward flow are strong before 250 s and the debris moves northeastward after passing the intersection. However, after 250 s, no movement occurs in the north–south direction because the eastward flow is dominant. No such clear tendency is evident in the results of either numerical model. Furthermore, the debris in the CC + SC model (Fig. 12(b)) passes the group of buildings because collision detection is conducted at only one point despite the multiple collision points between the debris and the buildings. Additionally, this passing occurs even though the water level at the top of buildings is less than the sum of the water level at the debris center and the draft depth. In the LC + MC model (Fig. 12(c)), debris does not pass between the buildings because the revised model maintains the non-contact condition with multiple collision points. However, no movement of debris to the top of the buildings occurs, unlike in the experiment. Such movement of debris to the higher elevated topography is observed in the FD case despite the small water level. In the FD case, movement from the sea to the land area occurs at the shoreline on the east side of the channel. These discrepancies between the experiment and the numerical models, analyzed in detail in the Discussion section, are attributable to the limitation of the planar two-dimensional model for debris motion.

4.4. Statistical characteristics of debris motion

Various previous studies have highlighted the importance of the uncertainty of debris behavior in hazard assessment (e.g., Kihara and Kaida, 2020; Ayca and Lynett, 2021; Xiong et al., 2022). In this part, we analyze the statistical characteristics of the trajectories and the moving velocity distribution, which is essential in the probabilistic assessment of debris. The differences in the debris motion between the CC + SC model and the LC + MC model are evident in the FD case. Fig. 14 shows the positions of the passage of the debris in north–south cross-sections (white dotted lines), and the mean, median, and standard deviation are shown in each cross-section. The mean position in the LC + MC model (green dotted line) differs substantially from that of the CC + SC model (blue dotted line), but is similar to that of the experimental results (red dotted line). As mentioned earlier, local contact between the debris bottom and the seafloor occurs immediately after the start of movement in the experiment, which causes rotational motion of the debris. Owing to the rotational effect, the main direction of movement of the debris is not parallel to the direction of the flow but to the southeast direction in the channel. Therefore, the numerical results of the LC + MC model improve the accuracy of the mean position by considering the local contact effect. To quantify the improvement of debris behavior, the relative error of the mean position for each cross-section is estimated. The difference between the experiment and the CC + SC model is evaluated as the reference value at the leftmost cross-section ($X = 1.8$ m, cross-section #1). The relative error in the CC + SC model is always >50%, whereas it is around 10%–25% in the LC + MC model.

Improvements of the numerical results by the LC + MC model are also observed for other statistical values, as shown in Fig. 14(a). In the CC + SC model, the mean position is closer to the experimental value as the cross-section is passed, but there is little change in the median value. Furthermore, the median is always to the north of the mean in the CC + SC model, unlike the experimental results. Because of the large distribution in the north–south direction, the standard deviation in the CC + SC model is overestimated in comparison with the experiment. On the other hand, the median values, the magnitude of the standard deviation, and the mean values are closer to the experimental results of the LC + MC model. We found that the revised model also improves not only the initial rotation, trajectories, and the final position, as shown in subsection 4.2, but also the statistical characteristics in the FD case. In the LD case (Fig. 14(b)), the mean position and the standard deviation are improved at the second cross-section. On the other hand, the debris in the CC + SC model moves without interference with the buildings, resulting in larger errors in the mean position and the standard deviation at the second cross-section. However, there is no significant difference between the two numerical models except for the abovementioned

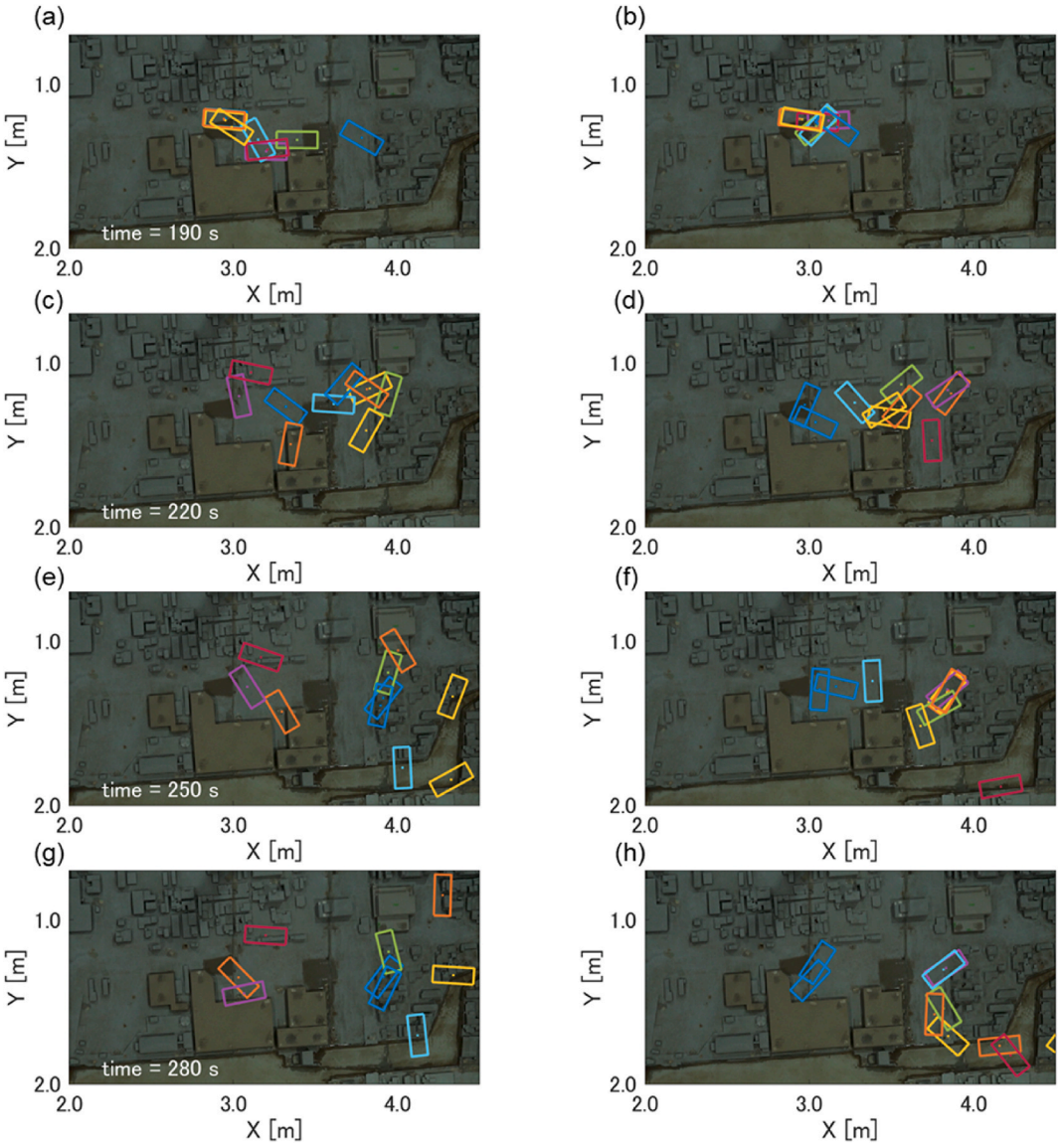

Fig. 11. Snapshot of modeled debris motion in the LD case at 190, 220, 250, and 280 s (color boxes: positions of debris, left column: CC + SC model, right column: LC + MC model).

characteristic. This might be because the topography of this area is relatively flat and the debris is not substantially affected by local contact that can lead to additional rotational motion.

Next, we mention the statistical characteristics of debris velocity. Fig. 15 shows the distribution of the moving velocities, similar to Fig. 14. In the FD case (Fig. 15(a)), the variation of moving velocity in the LC + MC model in the early stages of movement is larger than that in both the experiment and the CC + SC model. The difference is attributable to the timing of the release of the debris from contact with the seafloor and the subsequent acceleration. Both numerical models overestimate the debris velocities in the experiment at the second cross-section, i.e., the model improvement causes little difference in their distributions. In the LD case (Fig. 15(b)), the revised friction model suppresses the velocity increase in the early stages of movement, which is closer to the experimental results. We mentioned that local contact does not substantially affect the additional rotational motion in terms of debris position. In contrast, local contact does affect debris velocity. However, in the subsequent cross-sections, there is no notable difference between the two numerical models.

Summarizing the results of this section, the accuracy of debris position is enhanced by the model improvement because the rotational motion associated with local contact and the interference with buildings are important factors in determining the direction of debris movement in the local flow field. However, the accuracy of the debris velocity is not improved because it depends on the accuracy of the fluid velocity and evaluation of the associated hydrodynamic forces.

5. Discussion

Based on the numerical results, we discuss 1) the effect of the local contact model, 2) the limitation of the STOC-DM model on the movement to the top of buildings, and 3) the sensitivity analysis results. First, we discuss the effects of the friction model on the increase of the initial rotation angle and the associated change. Fig. 16(a) shows the results of the experiment's initial rotation angle of the movement in the FD case. The median rotation angle is approximately 46° in 30 s before contact with the seafloor is released; however, the variation is large, with a maximum of approximately 64° and a minimum of 14°. Furthermore, there is a difference in the direction of movement between rotation angles of 20° or less and other angles according to the correlation between the direction of movement from the initial position and the maximum rotation angle shown in Fig. 16(c). For example, the two

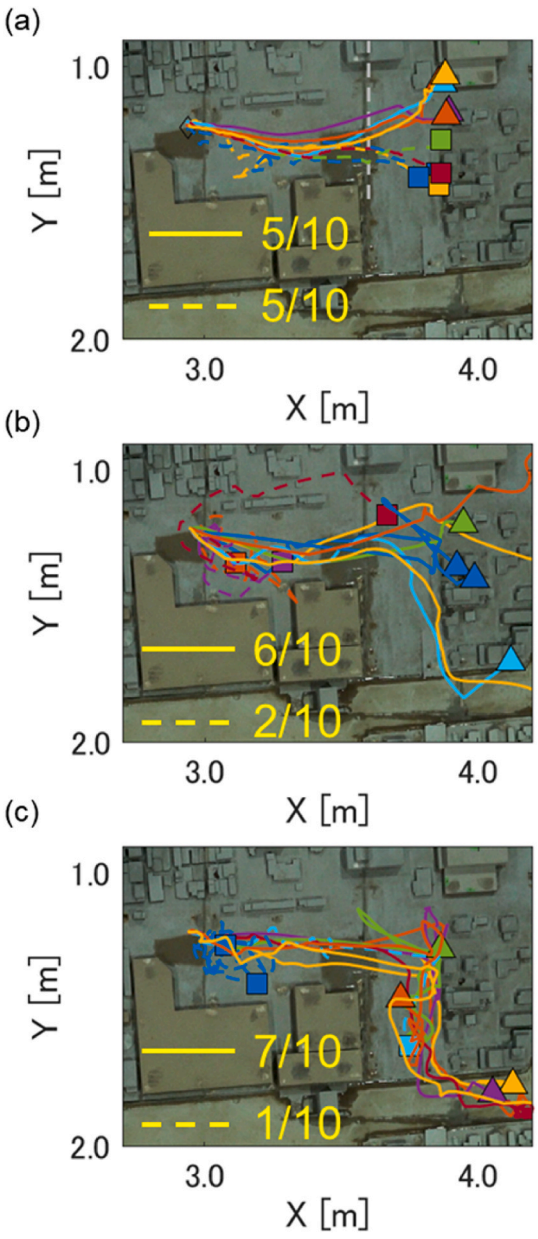

Fig. 12. Modeled debris trajectories in the LD case. Marker shows the arrival positions of the objects at 300 s (solid line with triangle marker: debris trajectories passing cross-section (white dotted line) before 250 s, dotted line with square marker: debris trajectories passing cross-section after 250 s, (a): experiment, (b): CC + SC model, (c): LC + MC model).

debris objects with rotation angles of 20° or less correspond to those that move on the north side of the channel in Fig. 9. This indicates that the rotation angle at the stage of the initial movement is a factor in determining the subsequent movement direction.

The numerical result shown in Fig. 16(b) indicates completely different tendencies with or without model improvement. The maximum rotation angle in the LC + MC model at the beginning of the movement is consistent with the experimental results. The revised model also improves all statistical indicators such as the median, mean, and maximum angles. Furthermore, the correlation between the movement direction and the maximum rotation angle is also improved, as shown in Fig. 16(c). The above results indicate that an increase in the rotation angle at the stage of the initial movement is essential for the southeast movement and that the improved contact model plays a role in this process.

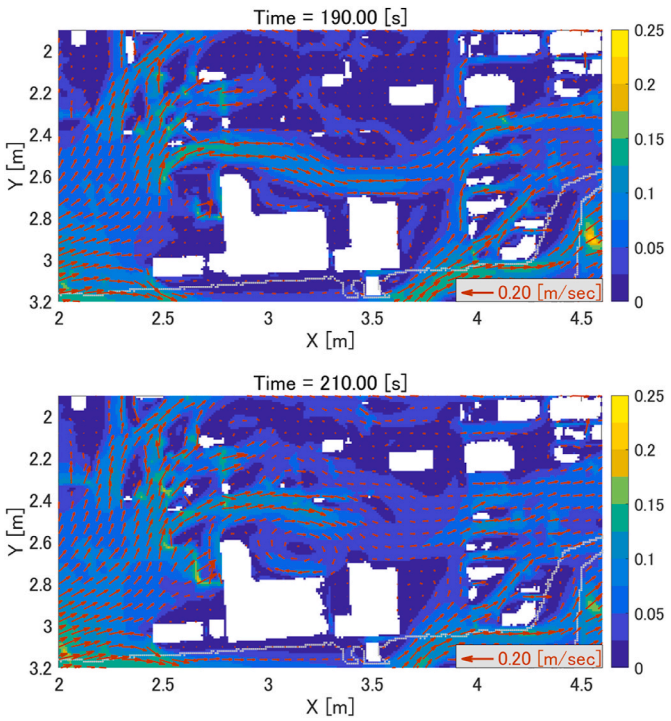

Fig. 13. Snapshot of flow velocity (contour with red arrows) around initial position of debris in the LD case. (upper: time at 190 s, lower: time at 210 s).

Second, we discuss the poor performance of the movement of debris on the land area from the shoreline along the east side of the channel in the FD case and the movement of debris to the top of the building in the LD case. In the vicinity of the group of buildings where the debris movement to the top occurs in the experiment, the water depth is higher than the top of the buildings after approximately 200 s in this numerical simulation. However, the water depth at the top of the buildings never exceeds the draft depth. The building height of the experiments is 4–5 cm, the maximum height at WG2 is 6 cm, and the draft depth of the debris is 2.5 cm. This means that debris cannot move onto the top of the buildings in the present model, even if the debris can maintain its position in front of the buildings and the water level reaches the maximum height. Another process is required for this vertical motion instead of the vertical motion due to the static equilibrium. One possibility is that the rotational motion around the horizontal axis might cause the debris to ride up to the corners of the buildings. Consequently, the debris would be easily affected by the vertical force. However, this process cannot be represented by the present STOC-DM model because it does not consider the rotational motion around the horizontal axis and it assumes static equilibrium for translational motion in the vertical direction. Therefore, further study of this motion is needed based on additional experiments and the use of the three-dimensional model.

Finally, we discuss the results of the sensitivity analysis of the debris motion. The above numerical results are performed considering uncertainties only in the fluid field. On the other hand, key parameters relating to debris such as the drag coefficient and the inertia coefficient should also be considered with uncertainty in the numerical model for debris transportation. Furthermore, it is also necessary to understand the sensitivity of the friction coefficient for the local contact model. In the following part, we present the numerical simulation results for debris when changing these parameters, and discuss especially the sensitivity to vortices in the port and the effect on debris velocity, which cannot reproduce the experimental results described in the previous section.

Sensitivity analysis was conducted for both the FD and the LD cases with different parameters: drag coefficients *Cd1* and *Cd2*, inertia

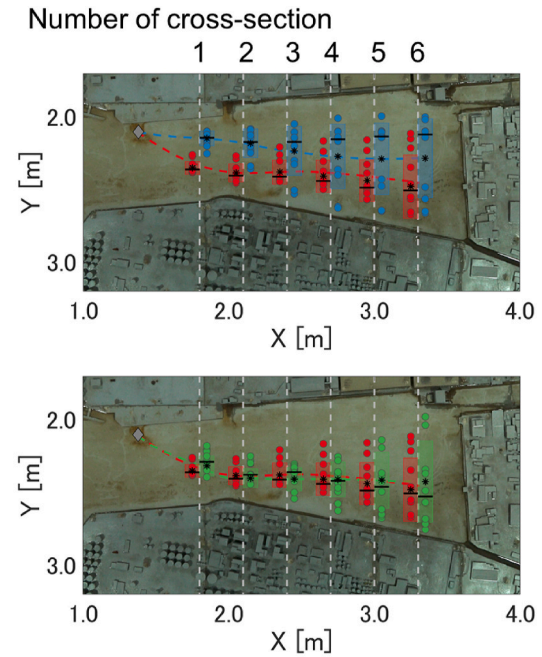

(a) FD case

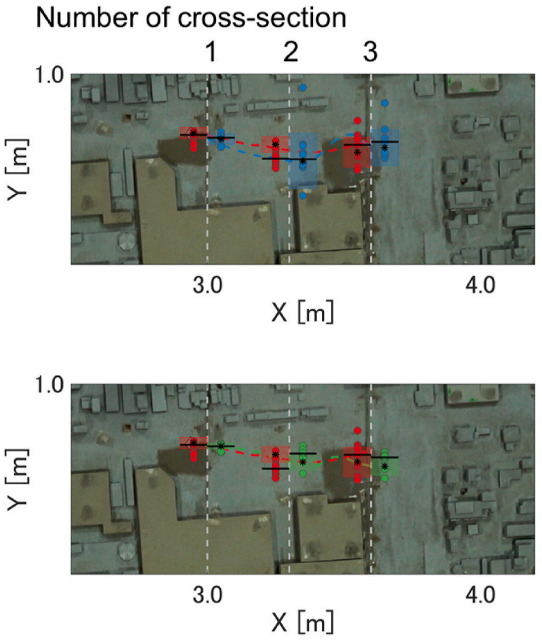

(b) LD case

Fig. 14. Statistical characteristics of debris positions during passage in the y-direction (mean: black asterisk, median: black line, and mean ± standard deviation: shading, red: experiment, blue: CC + SC model, green: LC + MC model).

(a) FD case

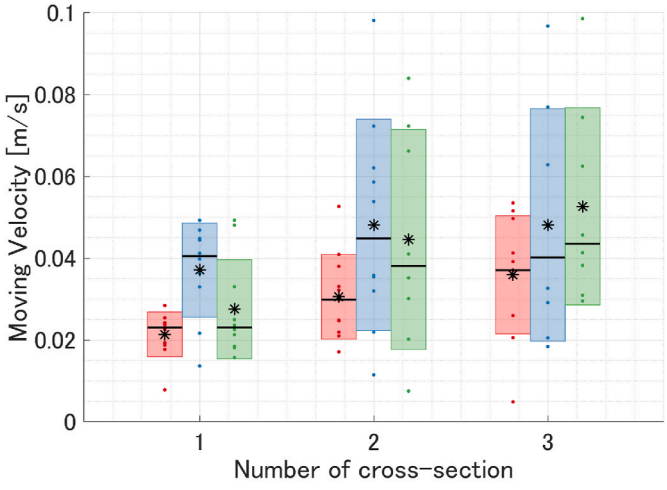

(b) LD case

Fig. 15. Statistical characteristics of debris moving velocity at each cross section (mean: black asterisk, median: black line, and mean ± standard deviation: shading, colors and markers correspond to Fig. 9).

coefficient *Cm*, and friction coefficient *Fc*. The drag coefficients *Cd1* and *Cd2* and the inertia coefficient *Cm* were included in the sensitivity analysis because they vary depending on the flow field conditions, such as the Reynolds number *Re*. In the STOC-DM model, when the relative velocity at the point of force action is positive, *Cd1* is adopted for the drag coefficient. Conversely, *Cd2* is adopted for the drag coefficient when the flow is away from the debris. The friction coefficient *Fc* was included because it might affect the release conditions of the local contact model. To simplify the effect of each parameter in this analysis, the numerical debris simulations were performed by multiplying the control case coefficient by a factor of 1.5 or 1/1.5. For the control case, three major coefficients were established as follows: $Cd1 = 0.8$, $Cd2 = 0.4$, $Cm = 2.0$, and $Fc = 0.4$. These values are the same as those used in the Results section.

First, the sensitivity of each parameter to moving distance is analyzed. The time series of moving distances from the initial position is compared with the control case in Fig. 17. The relative error R to the control case calculated using Eq. (11) is also shown in Fig. 17:

$$R = \frac{Dis_i - Dis_{ctrl}}{Dis_{ctrl}}, \tag{11}$$

where Dis_i and Dis_{ctrl} are the distance in the numerical simulation when changing the parameter and the distance in the control case, respectively. It should be noted that this result represents the average of the debris numerical simulations using each of the 10 hydrodynamic numerical simulations with different conditions on wave generation. In the FD case, the distance is equally varied for all parameters. However, the tendency is different for each parameter. The variation is larger around 40–70 s in the case of different drag coefficients and inertia coefficients, because the sensitivity of these coefficients to the ambient flow is large,

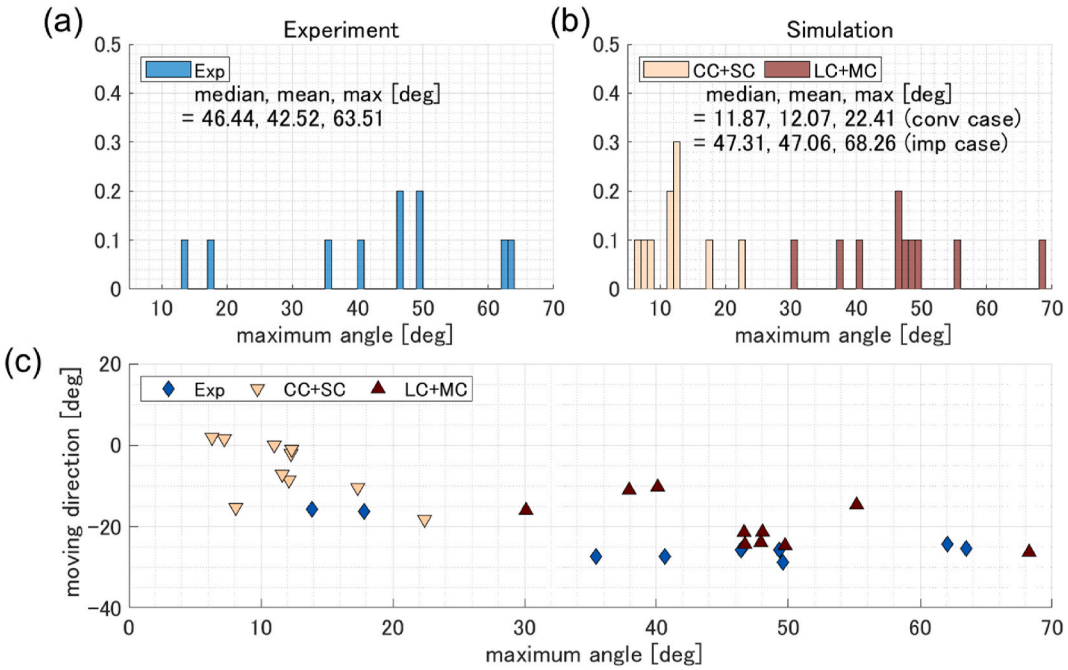

Fig. 16. Statistical characteristics of debris motion at initial stage of movement: (a) histogram of maximum rotation angle until 30 s after the experiment started, (b) numerical results, and (c) correlation of maximum angle and moving direction until 30 s after the experiment started. Counterclockwise is positive for the maximum angle, and northeast direction is positive for the movement from the initial location in the FD case.

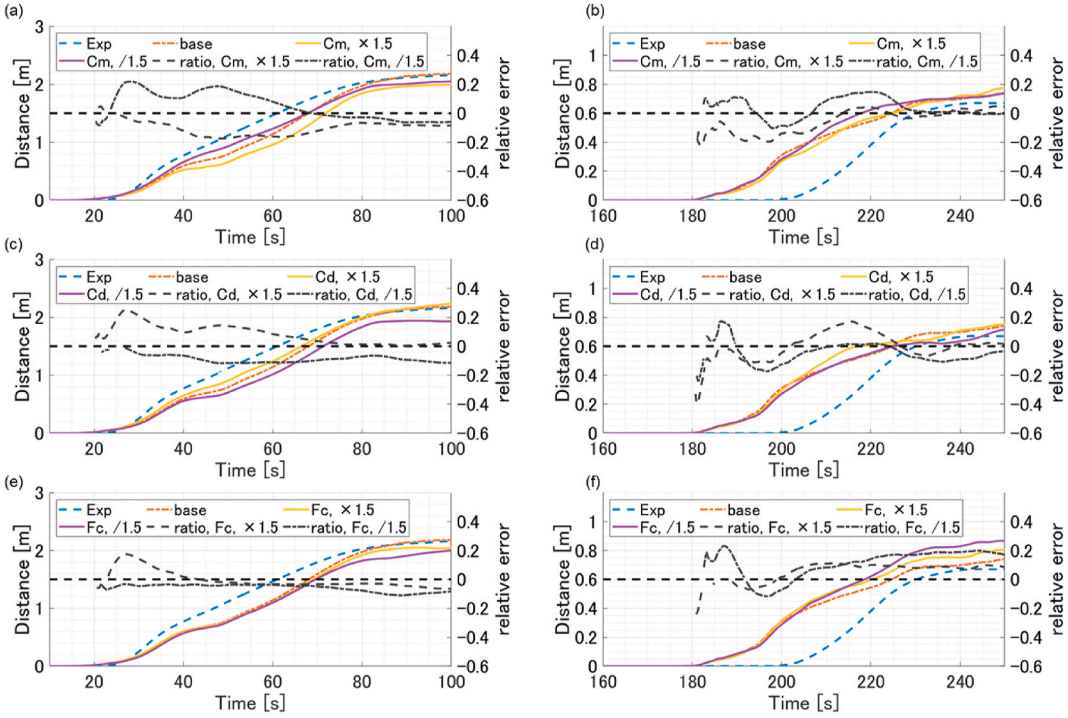

Fig. 17. Time series of moving distance (left axis, colored line) of debris from the initial position and relative error to control case (right axis, black line). Each panel shows the results of changing each parameter. (upper: Cm, middle: Cd, and lower: Fc, left column: FD case, right column: LD case).

as described below. On the other hand, there is little variation in the case of different friction coefficients, because the friction force acts only for a short period around the initial position of debris as shown in Fig. 8. However, slight variations due to the differences in friction coefficients at the initial stage of the movement increase over time, finally resulting in the same magnitude of variation as in the case of different drag coefficients and inertia coefficients. Furthermore, the relative error to the control case is approximately 10%–20% in all parameters, indicating that the average behavior does not highly depend on these coefficients.

In this part, we discuss why the sensitivity to the ambient flow is higher for the drag coefficients and the inertia coefficients, as described above. In the FD case, the numerical simulation with the inertia coefficient multiplied by 1/1.5 and the drag coefficient multiplied by 1.5 increases the distance by approximately 10%–20% relative to that in the

control case around 40–70 s. On the other hand, the differences among the parameters are smaller for the friction coefficient than for the other cases. The increase in the moving distance when the drag coefficient is multiplied by 1.5 is simply due to the increase in the hydrodynamic force acting on the debris. However, the same trend is not observed for the larger inertia coefficient. The reason for this discrepancy is the presence of vortices.

To clarify the influence of the vortices, the relationship between the spatial distribution of vorticity and the trajectories of each parameter is investigated in the two selected cases, as shown in Fig. 18. The separation of the incoming current causes vortex generation near the port entrance. Because the inertia force is proportional to the time derivative of the relative velocity, this value becomes greater in and around regions with a large change in flow. Thus, a large inertia force coefficient makes it easier to be trapped in a vortex. As shown in Fig. 18(a), the case with a large inertia coefficient (orange line) moves closest to the vortex, while the case with a small inertia coefficient moves away from the vortex. Debris with a small inertia coefficient not caught by the vortex moves in a direction toward the inner part of the bay, resulting in a larger distance in comparison with the case with a large inertia coefficient.

The magnitude of the variation in debris behavior between the different parameters depends on whether the debris is trapped in the vortex. For the case shown in Fig. 18(a), in which debris is trapped by the vortex, variation in debris movement depending on the different parameters is larger than that for the case shown in Fig. 18(b), in which debris is not trapped by the vortex. This difference in the magnitude of the variation between Fig. 18(a) and (b) is attributable to the difference in the flow field caused by small variations in wave conditions (approximately 1 mm standard deviation). Previous studies on numerical simulation of debris have often been conducted on the basis of adding perturbations to the initial positions and angles of the debris (e.g., Ayca and Lynett, 2021; Xiong et al., 2022). However, the results in this study might suggest the necessity of considering perturbations of the flow condition. Furthermore, as highlighted in previous studies (e.g., Borrero et al., 2015), the presence of a vortex is important in terms of the influence of the increase in hydrodynamic forces acting on debris objects. Moreover, the vortex is also important as a factor that causes variations in debris behavior.

Finally, we discuss the changes in the probability distribution of debris velocity using different parameters. Fig. 19 shows the probability density function (pdf) of the distribution of the debris velocity as it passes through the cross-sections shown in Fig. 14. The pdf is estimated using the kernel density estimation method. The solid yellow line in the figure indicates all numerical results obtained by considering the flow field variation and changing the debris parameters. The red dashed line indicates the results of the control case in which the variation of the flow field is considered. In comparison with the control case in which only variation in the flow field is considered, the distribution of debris velocity is improved and closer to that of the experimental results. This suggests that rather than considering the variability of either the flow or the debris separately, their variability should be considered concurrently. However, the sensitivity analysis in this numerical simulation only multiplies the selected parameters by a selected factor, and a more detailed analysis is needed in the future.

6. Conclusions

In this study, the STOC-DM debris transport model was improved on a collision model that can maintain a non-contact condition when debris collides with multiple structures at multiple points and on a local contact model that can account for the rotational motion when part of the bottom of a debris object is in contact with the ground or seafloor. The results from numerical simulations of debris movement using the improved model were compared with experimental results obtained

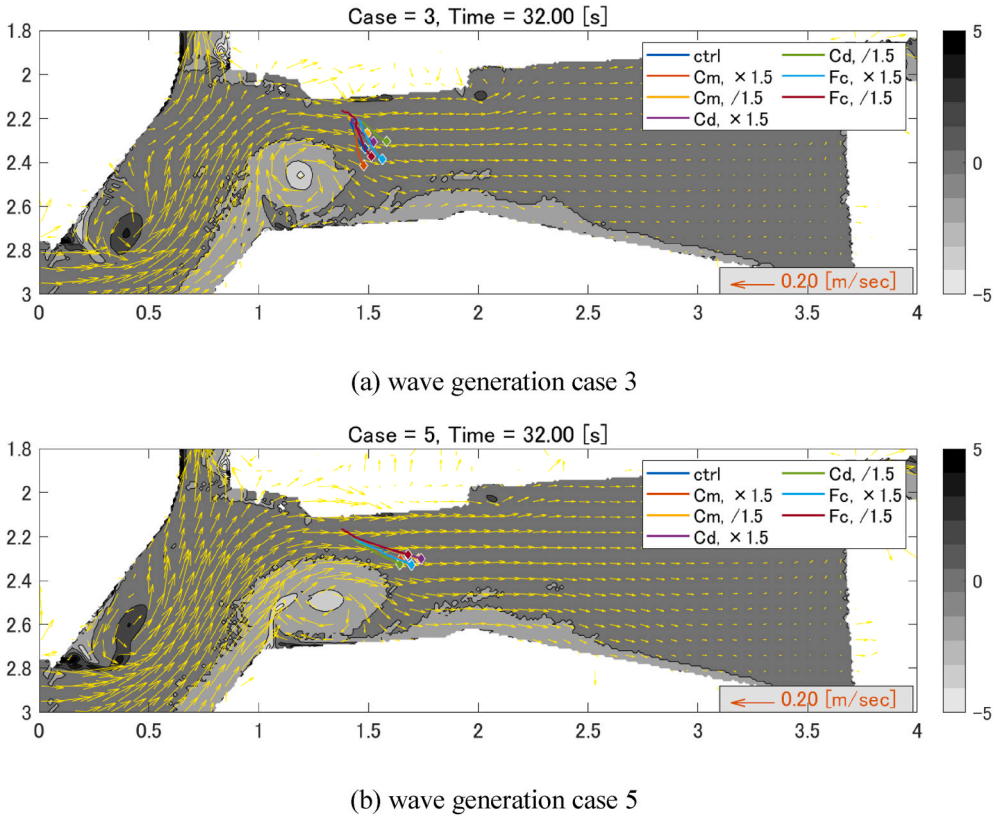

Fig. 18. Debris trajectories until 32 s from initial position in the FD case (colored line: debris trajectory with different parameter, contour: the spatial distribution of vorticity, yellow vector: flow velocity).

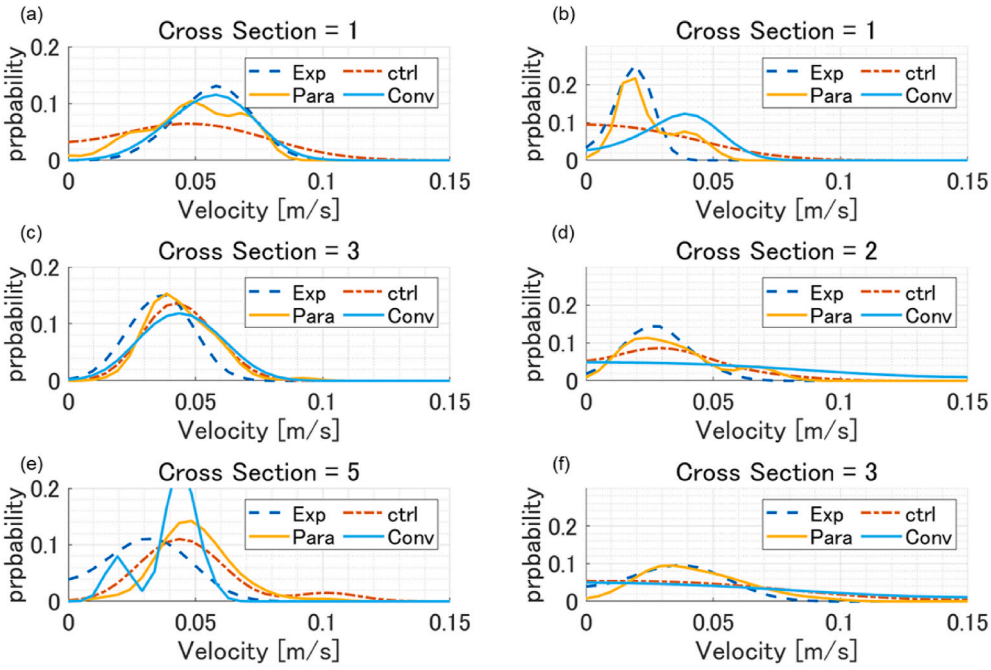

Fig. 19. Estimated pdf of moving velocity passing through each cross section. (Blue dotted line: experiment, red dashed line: control case, same as the LC + MC model results shown in Fig. 10, yellow solid line: all numerical results by the LC + MC model, light blue solid line: result of the CC + SC model, same as the CC + SC model results shown in Fig. 10, left column: FD case, right column: LD case).

using a physical city model simulating an actual port and urban area to verify the model accuracy. Ten hydrodynamic numerical simulations were performed with the data of 10 wave generation cases obtained in the experiment as boundary conditions. The initial positions and angles of the debris objects were fixed in the numerical simulations, i.e., numerical simulations of the debris were performed considering only the variation of the flow field. Although the numerical model effectively maintains the movement of debris in the urban area in terms of non-contact with the buildings, a problem was found with the reproducibility of debris movement to the tops of the buildings. The addition of consideration of the rotational motion associated with the local contact of the debris with the seafloor results in a change in the direction of movement owing to increase in the rotation angle. Consequently, it improved both the passing locations and the position of its final destination. However, even with the above improvements, the passing velocities at both the flume cross-section and the road cross-section are inconsistent with the experimental results. Further research is needed to validate the accuracy of the flow velocity on the complex city model and the accuracy of the evaluation equations for the hydrodynamic forces acting on debris.

Sensitivity analysis was conducted for three parameters used in the debris transport model: the drag coefficient *Cd*, inertia coefficient *Cm*, and friction coefficient *Fc*. By investigating the characteristics of debris behavior attributable to variation in the magnitude of these parameters, it was found that the presence of vortices affects debris behavior, and that the inertia coefficient *Cm* is highly sensitive to such vortices. Furthermore, it was found that considering not only the variation of the flow field but also that of the debris parameter improves the velocity distribution, which cannot be improved by the revised numerical model. Therefore, future research will focus on specifics such as how to artificially provide variation in the flow field, which of the many parameters inherent in debris should be selected, and how large a variation should be provided.

CRediT authorship contribution statement

Yu Chida: Conceptualization, Investigation, Methodology, Software, Visualization, Writing – original draft. **Nobuhito Mori:** Funding acquisition, Resources, Supervision, Writing – review & editing.

Declaration of competing interest

The authors declare that they have no known competing financial interests or personal relationships that could have appeared to influence the work reported in this paper.

Data availability

Data will be made available on request.

Acknowledgments

This work was supported by JSPS KAKENHI Grant Numbers JP17K13002, and partially supported by the Core-to-Core Collaborative Research Program of the Earthquake Research Institute, the University of Tokyo, and the Disaster Prevention Research Institute, Kyoto University (2021-K-01). The authors are also grateful to N. Fukui (Tottori University), T. Yasuda, T. Yamamoto (Kansai University), A. Kennedy, Z. Zhang, A. Copp (University of Norte Dame), T. Hiraishi, and M. Kamo (Kyoto University) for conducting a series of experiments.

References

American Society of Civil Engineers, 2016. Minimum Design Loads and Associated Criteria for Buildings and Other Structures, ISBN 9780784414248. ASCE/SEI 7-16.

Ayca, A., Lynett, P.J., 2021. Modeling the motion of large vessels due to tsunami-induced currents. Ocean Eng. 236, 109487.

Borrero, J., 2005. Field survey of northern Sumatra and banda aceh, Indonesia after the tsunami and earthquake of 26 december 2004. Seismol Res. Lett. 76 (3), 309–318.

Borrero, J., Lynett, P.J., Kalligeris, N., 2015. Tsunami currents in ports. Phil.Trans.R.Soc. A 373, 20140372. https://doi.org/10.1098/rsta.2014.0372.

Chida, Y., Takagawa, T., 2019. Numerical study on the distribution characteristics of debris due to tsunami by using nondestructive and fragmented drift object. J. of JSCE, Ser. B2 (Coastal Eng.) 75 (2), I_445–I_450. https://doi.org/10.2208/kaigan.75.I_445 (in Japanese).

Chida, Y., Fukui, N., Mori, N., Yasuda, T., Yamamoto, T., 2020. Experimental study of drift objects using spatiotemporal data under complex velocity field. J. of JSCE, Ser.

B2 (Coastal Eng.) 76 (2), I_313–I_318. https://doi.org/10.2208/kaigan.76.2_I_313 (in Japanese).
Chida, Y., Fukui, N., Mori, N., Yasuda, T., 2021. Effects of accuracy of spatio-temporal computation of fluid model and differences in initial condition of drift simulation on the accuracy of drift model for actual topography. J. of JSCE, Ser. B2 (Coastal Eng.) 77 (2), I_331–I_336. https://doi.org/10.2208/kaigan.77.2_I_331 (in Japanese).
Fujii, N., Ohmori, M., Ikeya, T., Asakura, R., Takeda, T., Yanagisawa, K., 2005. Numerical simulation of tsunami drifting bodies in a harbor. Ann. J. Coas. Eng. 52, 296–300 (in Japanese).
Fukui, N., Mori, N., Chang, C.W., Chida, Y., Yasuda, T., Yamamoto, T., 2020. Experimental study of tsunami and storm surge inundation using coastal city model. J. of JSCE, Ser. B2 (Coastal Eng.) 76 (2), I_373–I_378. https://doi.org/10.2208/kaigan.76.2_I_373 (in Japanese).
Fukui, N., Chida, Y., Zhang, Z., Yasuda, T., Ho, T.C., Kennedy, A., Mori, N., 2022. Variations in building-resolving simulations of tsunami inundation in a coastal urban area. J. Waterw. Port, Coast. Ocean Eng. 148 (1), 04021044.
Goseberg, N., Stolle, J., Nistor, I., Shibayama, T., 2016. Experimental analysis of debris motion due the obstruction from fixed obstacles in tsunami-like flow conditions. Coast Eng. 35–49. https://doi.org/10.1016/j.coastaleng.2016.08.012.
Goto, T., 1983. Numerical simulation of spread of floating timbers. Proceedings of the 30th Japanese conference on coastal engineering, JSCE. In: Proceedings of Coastal Engineering. Japan Society of Civil Engineers, pp. 594–597. https://doi.org/10.2208/proce1970.30.594 (in Japanese).
Hiraishi, T., Yasuda, T., Mori, N., Azuma, R., Mase, H., Prasetyo, A., 2015. Characteristics of tsunami generator newly implemented with three generation modes. J. of JSCE, Ser. B2 (Coastal Eng.) 71 (2), I_349–I_354. https://doi.org/10.2208/kaigan.71.I_349 (in Japanese).
Ikeno, M., Takabatake, D., Kihara, N., Kaida, H., Miyagawa, Y., Shibayama, A., 2016. Improvement of collision force formula for woody debris by air-borne and hydraulic experiments. Coast Eng. J. 58, 1640022 https://doi.org/10.1142/S0578563416400222.
Ikeya, T., Asakura, R., Fujii, N., Omori, M., Takeda, T., Yanagisawa, K., 2005. Experiments on tsunami wave forces acting on floating structures and proposed evaluation methods. Proc. of Coastal Eng., JSCE 52, 761–765 (in Japanese).
Kaida, H., Kihara, N., 2016. The debris behavior on the tsunami inundation flow. In: Journal of Japan Society of Civil Engineers, Ser. B2 (Coastal Engineering), 72, pp. 1159–1164. https://doi.org/10.2208/kaigan.72.I_1159 inJapanese.
Kihara, N., Kaida, H., 2019. An application of semi-empirical physical model of tsunami-bore pressure on buildings. Front. Built. Environ. 5 https://doi.org/10.3389/fbuil.2019.00003.
Kihara, N., Kaida, H., 2020. Applicability of tracking simulations for probabilistic assessment of floating debris collision in tsunami inundation flow. Coast Eng. J. 62 (1), 69–84.
Kotani, M., Imamura, F., Shuto, N., 1998. Tsunami run-up simulation and damage estimation by using GIS. Proc. of Coastal Eng., JSCE 45, 356–360 (in Japanese).
Kumagai, K., 2013. Tsunami-induced debris of freight containers due to the 2011 off the pacific coast of Tohoku earthquake. J. Disaster. factSheets. 1–25.
Matsutomi, H., 1999. A practical formula for estimating impulsive force due to driftwoods and variation features of the impulsive force. J. Jpn. Soc. Civ. Eng. 621, 111–127. https://doi.org/10.2208/jscej.1999.621_111 (in Japanese).
Mori, N., Takahashi, T., Yasuda, T., Yanagisawa, H., 2011. Survey of 2011 Tohoku Earthquake Tsunami inundation and run-up. Geophys. Res. Lett. 38 (7) https://doi.org/10.1029/2011GL049210.
Naito, C., Cercone, C., Riggs, H.R., Cox, D., 2014. Procedure for site assessment of the potential for tsunami debris impact. J. Waterw. Port, Coast. Ocean Eng. 140, 2.
Nistor, I., Goseberg, N., Mikami, T., Shibayama, T., Stolle, J., Nakamura, R., 2016. Hydraulic experiments on debris dynamics over a horizontal plane. J. Waterw. Port, Coast. Ocean Eng., 04016022 https://doi.org/10.1061/(ASCE)WW.1943-5460.0000371.
Park, H., Cox, D., Lynett, P.J., Wiebe, D.M., Shin, S., 2013. Tsunami inundation modeling in constructed environments: a physical and numerical comparison of free-surface elevation, velocity, and momentum flux. Coast. Eng. 79, 9–21. https://doi.org/10.1016/j.coastaleng.2013.04.002.
Park, H., Cox, D.T., 2019. Effects of advection on predicting construction debris for vulnerability assessment under multi-hazard earthquake and tsunami. Coast. Eng. 153 https://doi.org/10.1016/j.coastaleng.2019.103541.
Park, H., Koh, M.J., Cox, D.T., Alam, M.S., Shin, S., 2021. Experimental study of debris transport driven by a tsunami-like wave: application for non-uniform density groups and obstacles. Coast. Eng. 166, 103867.
Riggs, H.R., Cox, D.T., Naito, C.J., Kobayashi, M.H., Piran Aghl, P., Ko, H.S., Khowitar, E., 2014. Experimental and analytical study of water-driven debris impact forces on structures. J. Offshore Mech. Arctic Eng. 136 (4).
Rueben, M., Cox, D., Holman, R., Shin, S., Stanley, J., 2015. Optical measure-ments of tsunami inundation and debris movement in a large-scale wave basin. J. Waterw. Port, Coast. Ocean Eng. 141, 04014029 https://doi.org/10.1061/(ASCE)WW.1943-5460.0000267.
Stolle, J., Goseberg, N., Nistor, I., Petriu, E., 2017. Probabilistic investigation and risk assessment of debris transport in extreme hydrodynamic conditions. J. Waterw. Port, Coast. Ocean Eng. (1), 04017039 https://doi.org/10.1061/(ASCE)WW.1943-5460.0000428.
Stolle, J., Takabatake, T., Nistor, I., Mikami, M., Nishizaki, S., Hamano, Go, Ishii, H., Shibayama, T., Goseberg, N., Petriu, E., 2018. Experimental investigation of debris damming loads under transient supercritical flow conditions. Coast. Eng. 139 https://doi.org/10.1016/j.coastaleng.2018.04.026.
Stolle, J., Takabatake, T., Hamano, G., Ishii, H., Iimura, K., Shibayama, T., Nistor, I., Goseberg, N., Petriu, E., 2019. Debris transport over a sloped surface in tsunami-like flow conditions. Coast Eng. J. 1–15.
Suga, Y., Koshimura, S., Kobayashi, E., 2013. Risk evaluation of drifting ship by tsunami. J. Disaster Res. 8 (4), 573–583.
The Federal Emergency Management Agency (FEMA), 2007. FEMA-325 Public Assistance Debris Management Guide.
Tomiczek, T., Prasetyo, A., Mori, N., Yasuda, T., Kennedy, A., 2016. Physical modelling of tsunami onshore propagation, peak pressures, and shielding effects in an urban building array. Coast. Eng. 117, 97–112. https://doi.org/10.1016/j.coastaleng.2016.07.003.
Tomita, T., Kakinuma, T., 2005. Storm surge and tsunami simulation in oceans and coastal areas (STOC). Rept. Port. Airport Res. Inst. 44 (2), 83–98 (in Japanese).
Tomita, T., Honda, K., 2010. Practical model to estimate drift motion of vessels by tsunami. Coast. Eng. Proc. 1 (32) https://doi.org/10.9753/icce.v32.management.27.
Xiong, Y., Liang, Q., Zheng, J., Stolle, J., Nistor, I., Wang, G., 2022. A fully coupled hydrodynamic-DEM model for simulating debris dynamics and impact forces. Ocean Eng. 255, 111468 https://doi.org/10.1016/j.oceaneng.2022.111468.